Results in Physics 57 (2024) 107415

Contents lists available at ScienceDirect

Results in Physics

journal homepage: www.elsevier.com/locate/rinp

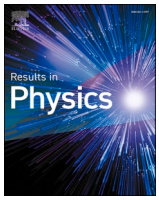

Band gap and THz optical adsorption of SnSe and $SnSe_2$ nanosheets on graphene: Negative dielectric constant of SnSe

Elaheh Mohebbi [a], Eleonora Pavoni [a], Luca Pierantoni [b], Pierluigi Stipa [a], Gian Marco Zampa [b], Emiliano Laudadio [a,*], Davide Mencarelli [b]

[a] Department of Science and Engineering of Matter, Environment and Urban Planning (SIMAU), Marche Polytechnic University, 60131 Ancona, Italy
[b] Information Engineering Department, Marche Polytechnic University, 60131 Ancona, Italy

ARTICLE INFO

Keywords:
First-principle calculation
2D materials
SnSe
$SnSe_2$
Graphene
THz frequency
Electronic and optical properties

ABSTRACT

Density functional theory (DFT) calculations have been used to investigate physical–chemical sensing of various proposed interfaces as SnSe@Graphene, $SnSe_2$@Graphene, Graphene@SnSe@Graphene, and Graphene@$SnSe_2$@Graphene, where dispersion corrections have been included to taken into account the vdW interactions between the layers. Initially, we predicted the electronic structures, mobility and carrier concentrations (cc) of SnSe and $SnSe_2$ structures. Using different methodology, the outcomes have confirmed the semiconductor properties of SnSe and $SnSe_2$ with indirect bandgap of 1.20 eV and 0.94 eV calculated by Generalized Gradient Approximation (GGA) and MetaGGA (MGGA) adopted with Perdew-Burke-Ernzerhof (PBE) functional, while hybrid Heyd-Scuseria-Ernzerhof (HSE) hybrid functional overestimated the experimental observations for both materials. Room temperature high mobility and cc have predicted by 126×10^3 cm^2V^{-1} s^{-1} with cc of 1.3×10^{13} cm^3 for a two layers SnSe and 69×10^3 cm^2V^{-1} s^{-1} with cc of 4.2×10^{18} cm^3 for three layers $SnSe_2$. Optical absorption spectrum revealed that the presence of two peaks at 60 THz and 48 THz with the intensity of 89879 cm^{-1} and 34504 cm^{-1} for interfaces including two layers of graphene. More interestingly, dielectric constant calculations showed that the transfer of carriers between graphene layers and SnSe in Graphene@SnSe@Graphene interface with absorption peak shifted to 24 THz along the in-plane direction and negative dielectric constants in the range of 24–169 THz, showing the effect of light-trapping through plasmonic.

Introduction

Two-dimensional (2D) materials can vary in terms of their physical properties and, hence, are often attractive in combinations for technological applications [1–5]. Among this class of materials, metal chalcogenides such as SnSe and $SnSe_2$ have prominent electrical, optical and electronic properties which make them potential candidates for applications in photovoltaic [6], photo-converter devices [7], memory devices [8], materials for solar cells [9], radiation detectors [10], optoelectronics [11], thermoelectric and cheap raw materials [12], and batteries and supercapacitors [13]. However, one promising research is the development of graphene heterostructures or composites with polymer, organic/inorganic conductors and semiconductors, which have shown remarkable improvements in physical performance [14].

Recent efforts have concentrated on taking advantage of the individual properties of different 2D materials by fabricating heterostructures, which are vertical stacks of 2D layers of dissimilar materials held together by weak van der Waals (vdW) forces [15]. In fact, vertically stacked 2D multilayer structures have become a promising prototype for functionalized nanodevices due to their wide range of tuneable properties. Such heterostructures were successful remarkably leading to opening of a bandgap in graphene by inserting on hexagonal boron nitride (h-BN) without changing its electronic mobility [16], and also the high-performance large-scale devices and circuits based on Graphene/MoS_2 heterostructure showed that tunability of the graphene work function with electrostatic doping significantly improved the ohmic contact to MoS_2 [17]. More interestingly, the bandstructures of Graphene/MoS_2 has been twisted by different rotation angles indicated very different from each other, while in the cases of MoS_2/MoS_2 are very similar. The variation of band structure with rotation angle in graphene/MoS_2 is, indeed, originated by the misorientation-induced lattice strain and the sensitive band-strain

* Corresponding author.
E-mail addresses: e.mohebbi@staff.univpm.it (E. Mohebbi), e.pavoni@staff.univpm.it (E. Pavoni), p.stipa@staff.univpm.it (P. Stipa), e.laudadio@staff.univpm.it (E. Laudadio).

https://doi.org/10.1016/j.rinp.2024.107415
Received 21 November 2023; Received in revised form 26 January 2024; Accepted 28 January 2024
Available online 1 February 2024

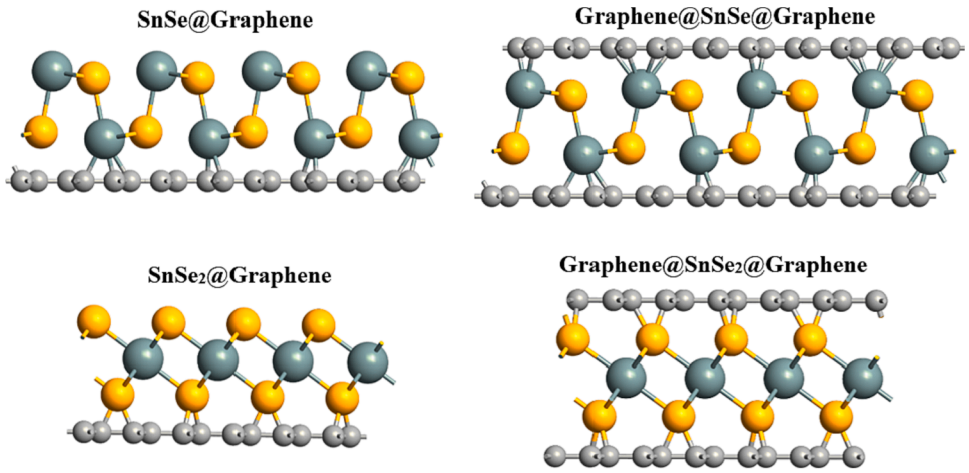

Fig. 1. Four different interfaces of the SnSe@Graphene, Graphene@SnSe@Graphene, $SnSe_2$@Graphene, and Graphene@$SnSe_2$@Graphene; the grey-dark, gold and grey-light sticks are the Sn, Se and carbon atoms respectively.

dependence to MoS_2 [18]. Moreover, the optical properties of graphene/WS_2 films have been enhanced compared to that of WS_2 and graphene, however with no evident dependency on thickness. On the other hand, the imaginary part of the optical susceptibility of graphene/WS_2 are approximately four times larger than that for WS_2 and two times larger than that for graphene [19]. In a recent study by Alsama et al. [20] dilatometer measurements indicated that in SnSe/Graphene Nanoplatelets (GNPs) sample the electrical performance was more stable than the pristine SnSe after consecutive thermal cycles. The obtained outcomes showed that homogeneously distributed graphene plays a significant role in improving the thermal stability of the SnSe-based nanocomposite.

In this study, we investigated the use of interlayer orientation between two different 2D materials as a tuning parameter for the electronic and optical properties of the free-standing layers and multilayers heterostructure. We presented different outcomes from vdW-corrected density functional theory (DFT) calculations on the effect of interlayer orientation on the electronic structure of the SnSe and $SnSe_2$ with graphene monolayers. We found that the relative orientation of graphene on below or/and upper part of SnSe and $SnSe_2$ monolayers strongly influences the value and type of the electronic structure of both materials, while having little effect on both the interlayer spacing. These results are relevant for heterostructures as potential devices in which exciton could be created in semiconductors SnSe and $SnSe_2$ sheets and graphene monolayers, and furthermore complete our previous related work in which the phonon scattering of acoustic and optical frequencies as well as charge contributions of each element in the lattices of SnSe and $SnSe_2$ monolayers have been investigated [21].

The main goal in this research is to develop nanostructures which can efficiently amplify THz waves based on surface plasmons in 2D materials which in their pristine structures they didn't show any THz adsorption. The fundamental attributes that underline this approach resides in the interaction between THz radiation and surface plasmons which provides amplification through an exchange of energy and electrons only by the properties of the gain medium. To this end, using numerical modelling and accurate simulations of the physics involved in THz amplification, we evaluated the critical properties such as electronic band gap, electron mobility, carrier concentration (cc), optical adsorption, and dielectric constants in the pristine monolayers and heterostructures. It is worthy to notice that the implementation of novel 2D materials for plasmonic amplification of THz sources will be needed as a gateway to develop this critical technology of THz frequency in the future.

Computational methods

The DFT calculations were performed using the Quantum ATK (QATK) [22] code. QATK software has implemented to characterize the properties of different materials and devices [23–25]. The Kohn–Sham (KS) formulation [26,27] has been resolved within the framework of the linear combinations of atomic orbitals (LCAO) basis set [28]. Norm-conserving (NC) PseudoDojo (PDj) pseudopotential (PPs) has adopted [29] to describe the valence orbitals approximating the core electrons. We performed complete optimization of the cell volume, shape, and atomic positions on the free-standing and heterostructures systems with the PBE [30] semi-local exchange–correlation (xc) functional. Numerical experiments have been carried out with inclusion of the dispersion corrections and by means of the Grimme method (DFT-D2) [31]. The band gap properties have been predicted by using the Generalized Gradient Approximation (GGA) [32], Meta-Generalized Gradient Approximation MetaGGA (MGGA) [33] and Heyd–Scuseria–Ernzerhof (HSE) [34] hybrid functionals to validate our computational approach by reproducing the structural and electronic properties of SnSe and $SnSe_2$ monolayers with the available experimental measurements. For atomic relaxations and bandstructure calculations, we used *k*-points mesh 13 × 10 × 1 and 12 × 12 × 1 grids for SnSe and $SnSe_2$, respectively. The structural optimization was carried out until the residual forces fell below 0.001 eV/Å. The electronic convergence tolerance was set to 10^{-5} eV. For all calculations, a kinetic energy cutoff of 120 Ry was chosen for the integration mesh [35,36].

After optimization of the SnSe, $SnSe_2$ and graphene monolayers, we modelled four heterostructures including of i) SnSe@Graphene, ii) $SnSe_2$@Graphene, iii) Graphene@SnSe@Graphene, and iv) Graphene@$SnSe_2$@Graphene on the basis of DFT calculations, while keeping the cell parameters under the self-consistent field convergence thresholds of 10^{-4}eV and 0.05 eV/Å for the total electronic energy and force, respectively. It is worthy to notice that we focus on how to enhance the electronic and optical properties of the SnSe and $SnSe_2$ structures for application in THz amplifications.

In QATK software, the response coefficients, the relative dielectric constant, ϵ_r, polarizability, α, and optical conductivity, σ, are related to the susceptibility calculated as [37,38],

$$\epsilon_r(\omega) = (1+\chi(\omega)), \tag{1}$$

$$\alpha(\omega) = V\epsilon_0\chi(\omega), \tag{2}$$

$$\sigma(\omega) = -i\omega\epsilon_0\chi(\omega), \tag{3}$$

Where χ, V and i refer to susceptibility tensor, volume and *i-th*

component (labelling electrons) of the momentum.

The optical absorption coefficient is related to the extinction coefficient through,

$$\alpha_a = 2\frac{\omega}{C}\mathrm{K} \tag{4}$$

While K is the extinction coefficient.

In terms of the real (ϵ_1) and imaginary parts (ϵ_2) of the dielectric constant as following Formula,

$$n = \sqrt{\frac{\sqrt{\epsilon_1^2+\epsilon_2^2}-\epsilon_1}{2}} \tag{5}$$

On the other hand, the mobility (μ) is related to the conductivity (σ) via,

$$\mu = \frac{\sigma}{ne} \tag{6}$$

where n is the carrier density and e is the electronic charge[39].

Results and discussion

Analysis of geometry and binding energy

While SnSe structure belongs to the orthorhombic lattice system (space group *Pnma*), having a folded lattice like black phosphorus, $SnSe_2$ possesses the hexagonal crystal system (space group *p-3m1*) (Fig. 1). The atomic bonding in 2D SnSe and $SnSe_2$ is covalent, while the interlayer is coupled by the vdW interactions. In this study, we simulated the heterostructures of SnSe and $SnSe_2$ monolayers on graphene monolayers with four simulations of SnSe@Graphene, $SnSe_2$@Graphene as well as Graphene@SnSe@Graphene, and Graphene@$SnSe_2$@Graphene by inserting the graphene monolayers on the below and upper parts of both materials, as shown in Fig. 1. After the optimization of all systems, the interlayer distance has measured between the graphene monolayers and the nearest C-Sn bond in the SnSe@Graphene and Graphene@SnSe@-Graphene and C-Se atoms for $SnSe_2$@Graphene and Graphene@$SnSe_2$@Graphene interfaces. The vertical space between the layers by adding the graphene monolayer were 2.16 Å and 1.84 Å for SnSe@Graphene and $SnSe_2$@Graphene, while in the cases of Graphene@SnSe@Graphene and Graphene@$SnSe_2$@Graphene hybrid materials the interlayer distances were reduced to 2.11 Å and 1.77 Å, respectively. However, the results from the electronic and optical properties indicate that interlayer orientation strictly effects the electronic structures of the semiconductors of SnSe and SnSe as well as metallic graphene, as we discuss later.

To assess the system stability, the binding energy (E_B) of four SnSe@Graphene, $SnSe_2$@Graphene, Graphene@SnSe@Graphene, and Graphene@$SnSe_2$@Graphene heterostructures has been calculated as Eq. (7),

$$\mathrm{E_B} = \frac{\mathrm{E(Interface)} - \mathrm{E(graphene)} - \mathrm{E(SnSe/SnSe_2)}}{\mathrm{N}} \tag{7}$$

where E(Interface) refers to total energy of each interface, E(graphene) and E(SnSe/$SnSe_2$) are the total energies of the graphene and SnSe or $SnSe_2$ monolayers, and N is the numbers of atoms in the supercell. The calculated E_B has obtained to be −0.53 eV, −0.70 eV, −0.63 eV and −1.09 eV for SnSe@Graphene, Graphene@SnSe@Graphene, $SnSe_2$@-Graphene, and Graphene@$SnSe_2$@Graphene interfaces, respectively. Among them, Graphene@$SnSe_2$@Graphene indicated more stable interface and as we discuss later, this SnSe heterostructure possesses higher electronic band gap value.

Electronic band gaps of SnSe and $SnSe_2$ monolayers

Before to consider the electronic properties of four different heterostructures as shown in Fig. 1, we calculated the electronic bandstructure and band gaps of both materials along with the high symmetry *k-mesh* directions in the first Brillouin zone (BZ). In order to verify our results, we computed the direct/indirect band gap properties of the SnSe and $SnSe_2$ monolayers using different methodologies as GGA, MGGA adopted with PBE xc, and HSE hybrid functional (Table 1). The results reveal that SnSe monolayer has a smaller direct/indirect band gap 1.41/1.20 eV by GGA with respect to 1.69/1.48 eV from MGGA, and higher values of 1.96/1.78 eV by HSE functional. The size of indirect bandgap computed with GGA/PBE is nearest to the published experimental value measured in Ref. [40] with the value of 1.3 eV. About the electronic properties of $SnSe_2$ nanosheet, the dependence of the electronic bandgap of the structure via applying different methodologies showed the equal trend with SnSe with lowest direct/indirect band gaps by GGA (1.09/0.75 eV), then MGGA (1.26/0.94 eV) and highest values obtained by hybrid HSE functional (1.77/1.44 eV), leading to the semiconducting character of both materials. According to the experimental results reported by Rajesh *et al.* [41], Lu *et al.* [42] and Kumar *et al.* [43] the indirect band gap of $SnSe_2$ has reported to be 0.9 eV, 1.00 eV and 1.02 eV, respectively, in consistency with our estimated band gap by MGGA. These outcomes imply that conventional methodologies like GGA/PBE and MGGA/PBE not necessarily underestimate the bandgap of semiconductors, while HSE hybrid functional method in some cases provide a less accurate prediction of the bandgap. The band structure analysis for SnSe and $SnSe_2$ monolayers have reported here in Fig. 2 by the most accurate GGA and MGGA approaches, respectively.

Table 1
Electronic band gaps of the SnSe and $SnSe_2$ monolayers using different methodologies of GGA, MGGA and HSE.

2D material	GGA	MGGA	HSE
SnSe	Direct band gap = 1.40 eV Indirect band gap = 1.19 eV	Direct band gap = 1.69 eV Indirect band gap = 1.48 eV	Direct band gap = 1.96 eV Indirect band gap = 1.78 eV
$SnSe_2$	Direct band gap = 1.09 eV Indirect band gap = 0.75 eV	Direct band gap = 1.26 eV Indirect band gap = 0.94 eV	Direct band gap = 1.77 eV Indirect band gap = 1.44 eV

Mobility and carrier concentrations

In Table 2, we illustrated the mobility and carrier concentration (cc) at different temperature of 100° K, 300° K and 500° K as well as Fermi energy (in eV) of monolayer, two layers, three layers, and four layers of SnSe and $SnSe_2$. The mobility of SnSe results higher than $SnSe_2$, moreover, by increasing the temperature from 100° K to 500° K the mobilities for all the material thicknesses were reduced while the cc values were increased. In details, the results show that SnSe and $SnSe_2$ monolayers can have the mobility of 98 × 10^3 cm^2V^{-1} s^{-1} and 84 × 10^3 cm^2V^{-1} s^{-1} at 100° K, whereas the cc at the same temperature indicated very low value for SnSe monolayer of 7.0 × 10^{-8} cm^3 and relatively higher value of 7.8 × 10^6 cm^3 for $SnSe_2$ monolayer. At 300° K and 500° K, we obtained the mobility decreasing from 43 × 10^3 cm^2V^{-1} s^{-1} with a cc of 2.1 × 10^{10} cm^3 to 32 × 10^3 cm^2V^{-1} s^{-1} at a cc of 1.3 × 10^{14} cm^3. The corresponding values for $SnSe_2$ have predicted 31 × 10^3 cm^2V^{-1}/21 × 10^3 cm^2V^{-1} with cc of 1.8 × 10^{15} cm^3/1.7 × 10^{17} cm^3 at 300° K/500° K, respectively.

Focusing on SnSe 2D material, the even layers shown higher mobilities than odd layers when we increase the thickness (Table 2). For instance, very high mobility of 361 × 10^3 cm^2V^{-1} s^{-1} and 343 × 10^3 cm^2V^{-1} s^{-1} can be observed for two layers and four layers thicknesses, while corresponding values at three layers material thickness has reduced to 316 × 10^3 cm^2V^{-1} s^{-1}. About the $SnSe_2$ structures, there is

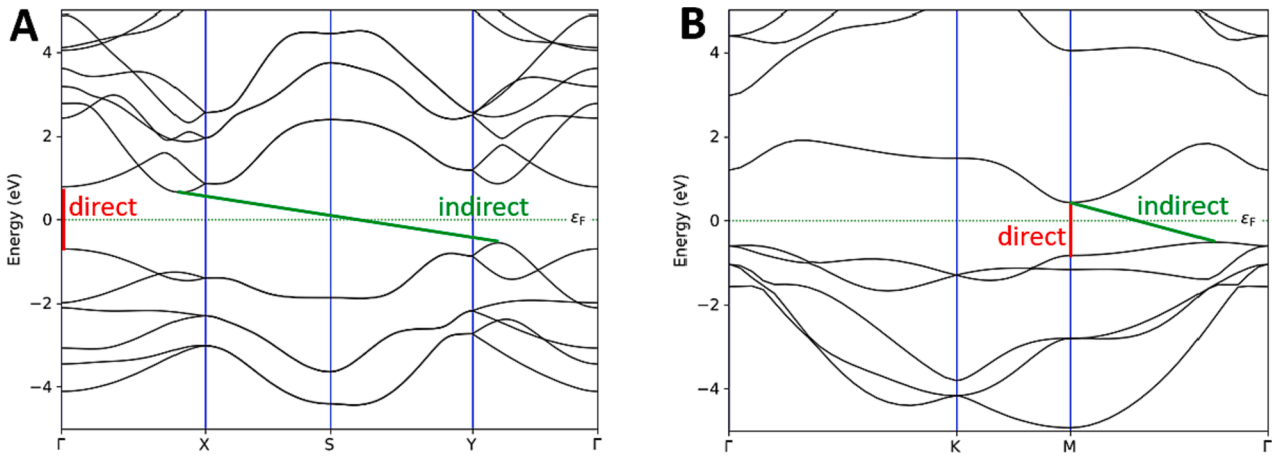

Fig. 2. Bandstructure of SnSe (A) and $SnSe_2$ (B) monolayers using different methodologies of GGA and MGGA, respectively, along the high symmetry directions in their first Brillouin zone; Fermi energy has set to be zero. Direct and indirect band gaps are coloured in red and green lines. (For interpretation of the references to colour in this figure legend, the reader is referred to the web version of this article.)

Table 2
Mobility ($\times 10^3$) and carrier concentration (cc) at different temperature of 100°K, 300°K and 500°K as well as Fermi energy (in eV) of monolayer, 2 layers, 3 layers, and 4 layers of the SnSe and $SnSe_2$. The units of Mobility and cc are $cm^2v^{-1}s^{-1}$and cm^3, respectively.

2D material	Thickness	100°K		300°K		500°K		E_f (eV)
		Mobility	cc	Mobility	cc	Mobility	cc	
SnSe	Monolayer	98	7.0×10^{-8}	43	2.1×10^{10}	32	1.3×10^{14}	−4.09
	2 layers	361	2.2×10^{13}	126	1.3×10^{13}	74	4.6×10^{15}	−4.07
	3 layers	316	6.0×10^{5}	104	2.7×10^{14}	56	4.3×10^{16}	−4.11
	4 layers	343	7.4×10^{7}	110	7.5×10^{14}	53	4.5×10^{16}	−4.13
$SnSe_2$	Monolayer	84	7.8×10^{6}	31	1.8×10^{15}	21	1.7×10^{17}	−5.59
	2 layers	180	6.4×10^{15}	61	1.4×10^{18}	38	7.1×10^{18}	−5.12
	3 layers	204	4.6×10^{17}	69	4.2×10^{18}	43	1.1×10^{19}	−5.10
	4 layers	173	7.5×10^{17}	61	5.7×10^{18}	40	1.3×10^{19}	−5.09

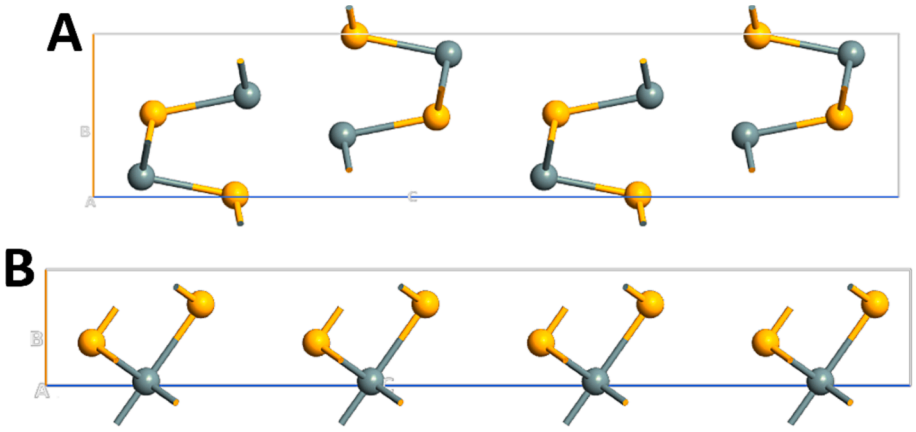

Fig. 3. Four layers thicknesses of SnSe (A) and $SnSe_2$ (B) structures.

not the same trend as SnSe and interestingly, a three layers material indicated higher mobilities especially respect to monolayer and four layers thicknesses. These differences between 2D SnSe and $SnSe_2$ nanostructures may be the reason of different positions of the layers by increasing the thickness. As shown in Fig. 3, for a four layers thickness of SnSe, the alignment of odd layers is different from the even layers, while in $SnSe_2$ material all the layers are positioned in the same line. This non monotonic trend in SnSe structure shows an odd–even quantum confinement effect, because the interplay of spin–orbit coupling and lack of inversion symmetry in odd-numbered layer structures results in anisotropic spin splitting of the energy bands. This can be explained in terms of the asymmetry of the crystal space group and a spin–orbit coupling effect. So, the results related to geometry, lattice system and band structure can significantly influence the transport properties and mobility in SnSe monolayer and few-layers. For sure, we require to consider other factors that are crucial for carrier mobility such as large elastic moduli, small effective mass, and small deformation potentials, in the near future for this study.

While previous DFT calculations and experimental evidence have only considered monolayers or crystalline structures at room

Table 3
Band gap (eV) for four heterostructure systems of SnSe@Graphene, $SnSe_2$@-Graphene, Graphene@SnSe@Graphene and Graphene@$SnSe_2$@Graphene along the z direction in their supercell including the valence band maximum (VBM) and conduction band minimum values (CBM); Fermi energy has set to be zero.

Interface System	Band gap	VBM	CBM
SnSe@Graphene	0.02	−0.018	0.001
$SnSe_2$@Graphene	0.07	−0.014	0.06
Graphene@SnSe@Graphene	0.2	−0.18	0.024
Graphene@$SnSe_2$@Graphene	1.08	−1.05	0.033

temperature of SnSe and $SnSe_2$, in this study we predicted how increasing the temperature as well as material thickness can change the mobility and cc of the structures. However, our findings strongly support the general conclusions made in different literatures. Zhou *et al.* [44] have so far achieved room-temperature value of 24×10^3 cm^2V^{-1} s^{-1} for SnSe, and experimental measurement of Wang *et al.* [45], has reported a cc of 4.2×10^{17} cm^3. About the $SnSe_2$, Linag *et al.* [46], has found the carrier mobility of $SnSe_2$ monolayer in the presence of hexagonal boron nitride (h-BN) up to 10^4 cm^2 V^{-1} s^{-1}. In addition, Liu *et al.* [47], in an experimental study show the cc of 1.9×10^{18} cm^3 at 300° K in which is in a good consistency with two layers $SnSe_2$ thickness considered in this research. According to the changing of Fermi energies with respect to increasing the materials thickness, while in SnSe by enhancing the layers the Fermi level shifted to the negative energies, in $SnSe_2$ the opposite trend was observed, with more positive values.

Electronic and optical properties of heterostructure systems

Bandstructure and band gap calculations

The Table 3 shows the band gaps and corresponding valence band maximum (VBM) and conduction band minimum (CBM) values related to SnSe@Graphene, $SnSe_2$@Graphene, Graphene@SnSe@Graphene, and Graphene@$SnSe_2$@Graphene, obtained from bandstructures calculations along the z direction in their supercells (Fig. 4) for each system. By adding the graphene layers putting on both sides of SnSe and $SnSe_2$ the band gap have been enhanced in two cases of SnSe and $SnSe_2$, however, $SnSe_2$@Graphene and Graphene@$SnSe_2$@Graphene shown higher band gaps than SnSe@Graphene and Graphene@SnSe@-Graphene. The total bandgap values have predicted to be 0.02 eV and 0.07 eV for SnSe@Graphene and $SnSe_2$@Graphene hybrid materials, and higher values of 0.2 eV and 1.08 eV for Graphene@SnSe@Graphene and Graphene@$SnSe_2$@Graphene, respectively. Inspection to the valence and conduction bands in different systems (Table 3) reveal that SnSe@Graphene and Graphene@SnSe@Graphene have more density of charges in the valence region, whereas $SnSe_2$@Graphene and Graphene@$SnSe_2$@Graphene possess most contributions of the charges in conduction and valence bands, respectively. According to the results reported in section 3.1, by optimization of all four systems, the vertical distances between semiconductor-metallic layers in the case of SnSe heterostructures consist of SnSe@Graphene and Graphene@SnSe@-Graphene showed higher values of 2.16 Å and 2.11 Å, while $SnSe_2$@-Graphene and Graphene@$SnSe_2$@Graphene interfaces indicated the smaller interlayer distances of 1.84 Å and 1.77 Å, respectively. These equilibrium distances between the layers can efficiently influence the electronic band diagram of the interfaces (as seen in VMB and CMB values in Table 3), and SnSe@Graphene with the highest interlayer distance and Graphene@$SnSe_2$@Graphene with the lowest one revealed the higher and lower band gaps between them. However, Graphene@$SnSe_2$@Graphene can be considered as a wide-band gap insulator among graphene heterostructures.

Inspection of Fig. 4 indicates how much the bandstructure of SnSe and $SnSe_2$ monolayers have been changed after the interfaces on SnSe@Graphene, $SnSe_2$@Graphene, Graphene@SnSe@Graphene and Graphene@$SnSe_2$@Graphene along the G-Z directions in their first BZ (along the z direction in their supercells). The band gap of pristine SnSe monolayer has changed from 1.20 eV before the adsorption (see section 3.2) to 1.76 eV after the adsorption on graphene monolayer, while this value has significantly reduced to 0.13 eV when two graphene monolayers have inserted on below and upper part of SnSe nanostructure. About the $SnSe_2$ mono-sheet which possesses the band gap of 0.94 eV in the pristine condition, the band gap has changed to 1.13 eV and 0.40 eV

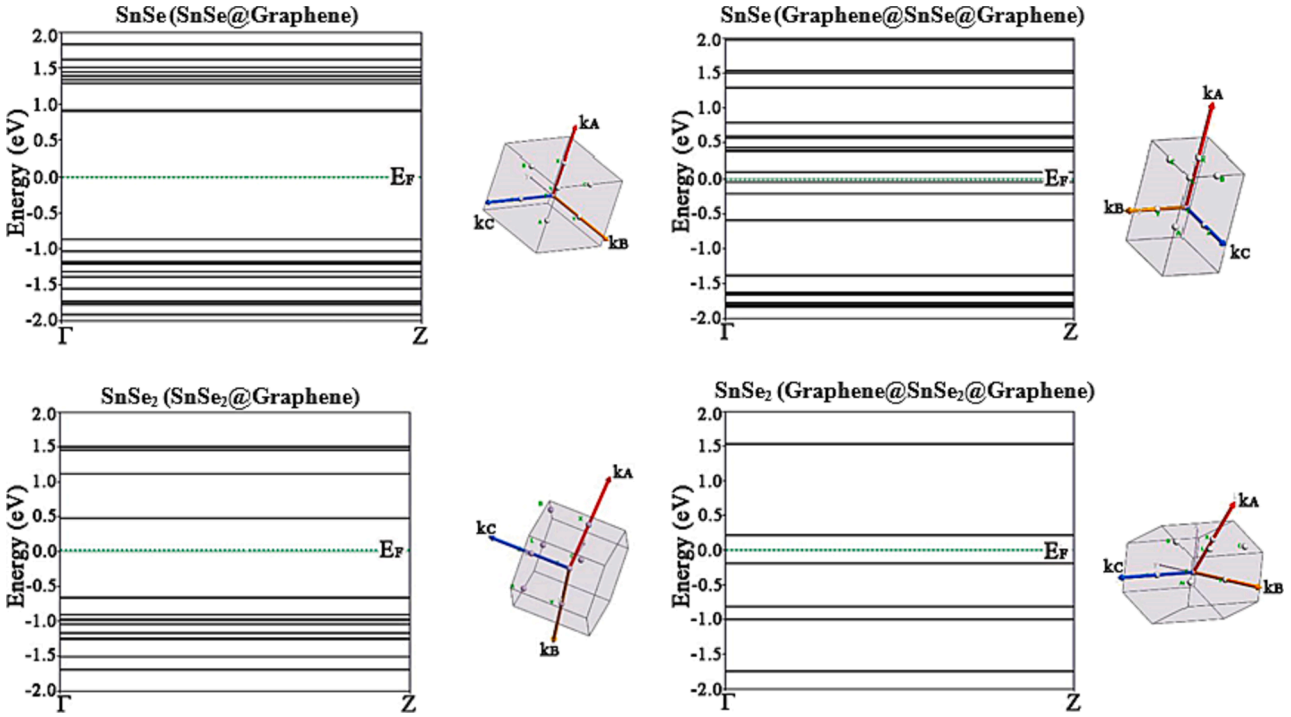

Fig. 4. Bandstructure of SnSe and $SnSe_2$ monolayers after the interfaces on graphene monolayer (SnSe@Graphene and $SnSe_2$@Graphene), and both layers of graphene (Graphene@SnSe@Graphene and Graphene@$SnSe_2$@Graphene interfaces). First Brillouin zone corresponding to each interface has been shown.

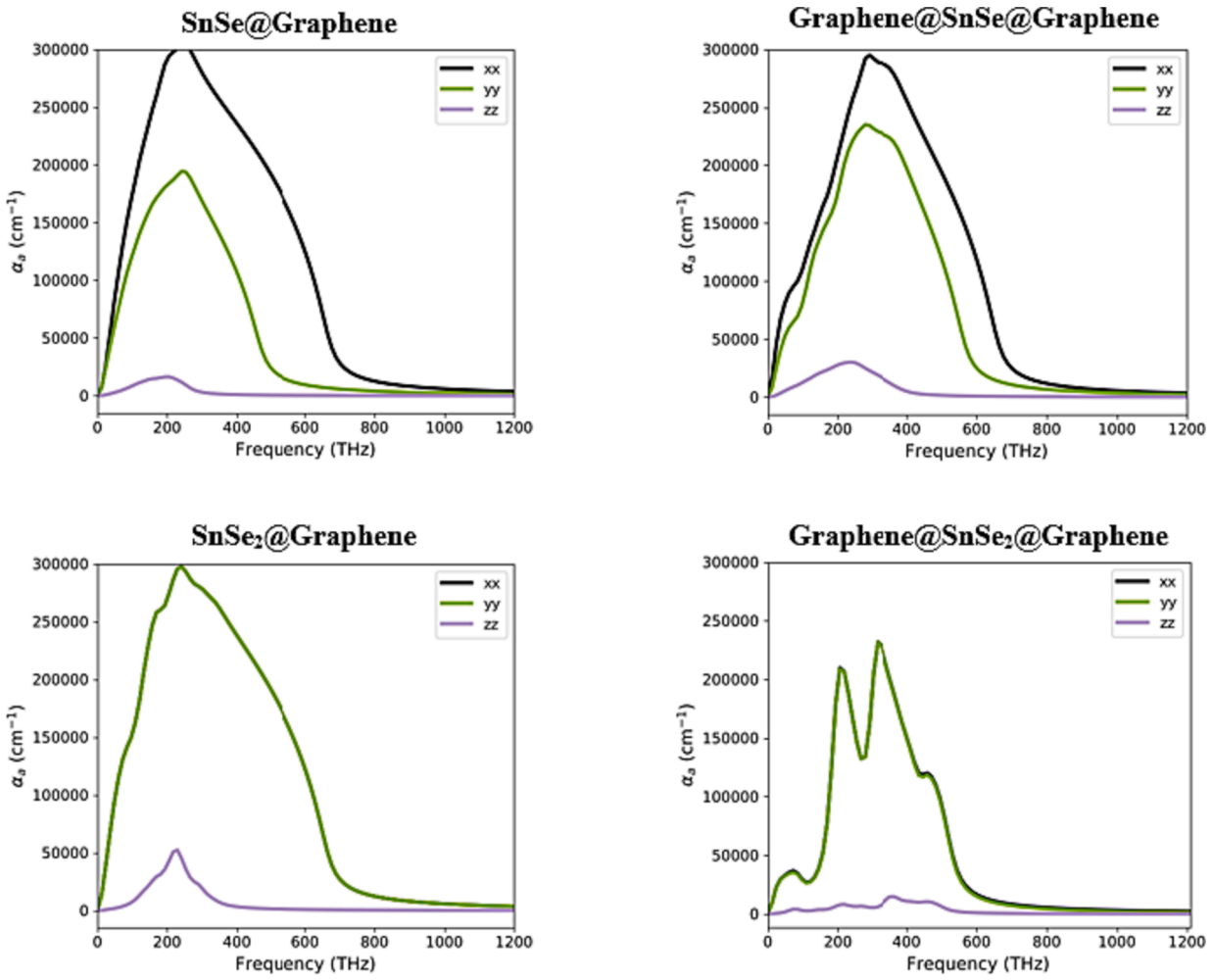

Fig. 5. Optical absorption spectra corresponding to SnSe@Graphene, $SnSe_2$@Graphene, Graphene@SnSe@Graphene, and Graphene@$SnSe_2$@Graphene interfaces, as a function of THz.

after inserting this material in modelled $SnSe_2$@Graphene and Graphene@$SnSe_2$@Graphene interfaces, respectively. These outcomes reveal the role of the carbon atoms in graphene monolayers in different orientations to change the electronic structure of these two 2D materials. Although, the simulated electronic band gaps have demonstrated that the graphene has still zero band gap after interfaces with SnSe and $SnSe_2$ monolayers, however, the electronic states near the Fermi level are mainly contributed by Sn-*d*, Se-*p*, and graphene π-system, which are responsible for electronic contribution in the energy band gaps of heterostructures. According to our results, graphene can narrowing or broadening the band gap of both SnSe and $SnSe_2$ monolayers due to metallic and semiconductor monolayer hybridization. Later, optical properties will reveal some predictions which explain these changing in the electronic structure of the interfaces.

Optical adsorption spectrum and dielectric constants

In this section, we reported adsorption coefficient and real and imaginary part of dielectric constants. The Fig. 5 indicates the absorption spectra for the four interfaces SnSe@Graphene, $SnSe_2$@Graphene, Graphene@SnSe@Graphene, and Graphene@$SnSe_2$@Graphene heterostructures in the wide range of 0–1200 THz frequencies. Investigating the data obtained from semi-local PBE calculations are computed along the *xx*-, *yy*- (in-plane), and *zz*-direction (out-of-plane) polarizations.

The maximum adsorption spectra approximated are 304480 cm^{-1} and 292090 cm^{-1} at 265 THz and 278 THz for SnSe@Graphene and Graphene@SnSe@Graphene, and 297428 cm^{-1} and 231690 cm^{-1} at 297 THz and 231 THz for $SnSe_2$@Graphene and Graphene@$SnSe_2$@-Graphene along the in-plane directions, respectively. Based on this figure and the range of photon energy (THz), two small peaks can be observed for Graphene@SnSe@Graphene and Graphene@$SnSe_2$@-Graphene multilayers in the 60 THz and 48 THz with the intensity of 89879 cm^{-1} and 34504 cm^{-1}, respectively, whereas these two peaks are not presented in the optical absorption spectrum of SnSe@Graphene and $SnSe_2$@Graphene. The outcomes also indicated that the main peaks of absorption spectra of $SnSe_2$@Graphene are completely different from other three systems with four separated peaks along the in-plane directions. Overall, the comparison of the four systems reveal that the absorption coefficient was more strengthened in the interfaces modelled by two layers of graphene at low frequencies in THz range, resulting from changing the optical properties of SnSe and $SnSe_2$ semiconductors, as we discuss later.

In the next step, optical absorption spectra for separated monolayers of SnSe and $SnSe_2$ materials before and after the interfaces on graphene monolayers have been compared, as a function of THz in the range of 0–400, as reported in Fig. 6. The outcomes have been predicted for SnSe nanostructure reveal that, the main first peak has shifted to higher frequencies from 350 THz and 302 THz for in-plane directions to 362 THz and 398 THz after the absorption on graphene monolayers, respectively. However, when SnSe sandwiched between two layers of the graphene, its adsorption peak has transferred to very low frequencies at 24 THz and 36 THz along the same directions resulting from its small band gap, as we discussed in section 3.4.1. The results have evaluated for $SnSe_2$

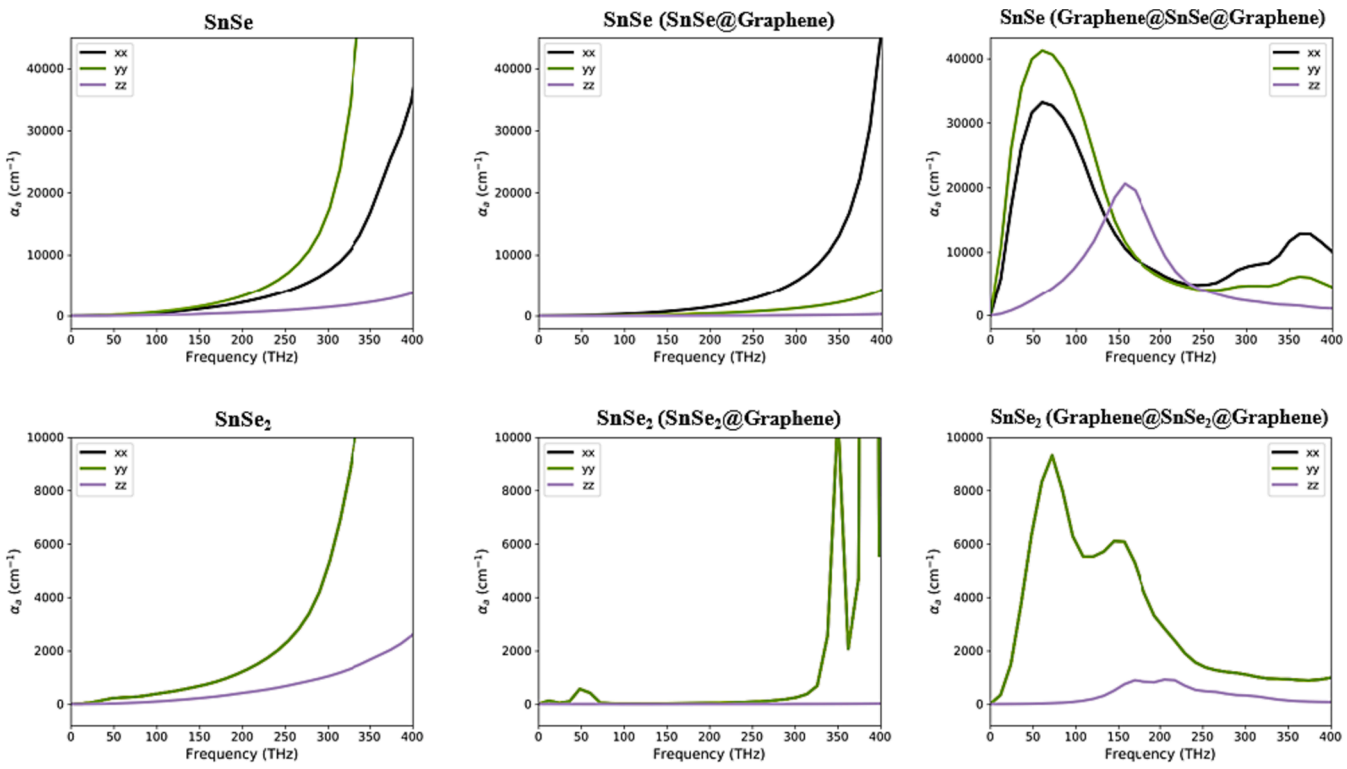

Fig. 6. Optical absorption spectra for SnSe and $SnSe_2$ monolayers before and after the interfaces on graphene monolayer (SnSe@Graphene and $SnSe_2$@Graphene), and a both layers of graphene (Graphene@SnSe@Graphene and Graphene@$SnSe_2$@Graphene interfaces), as a function of THz.

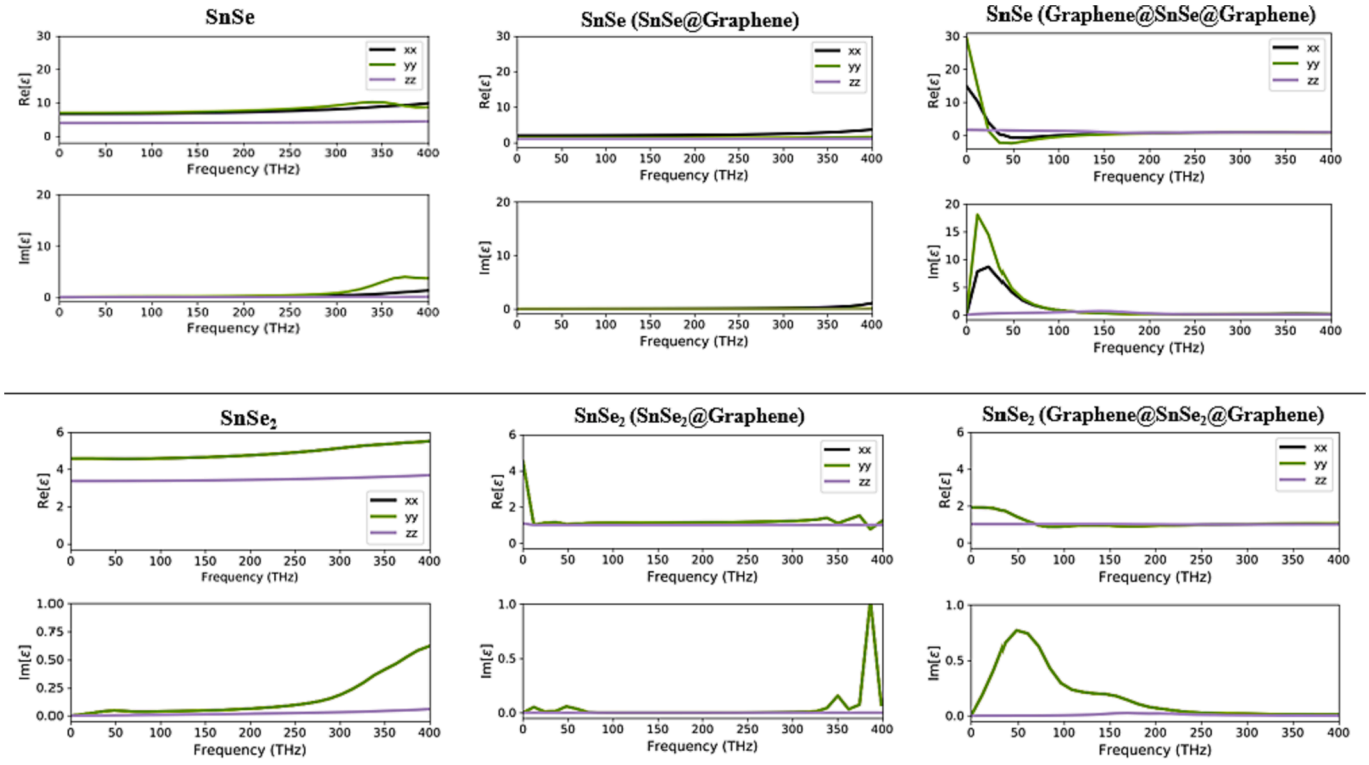

Fig. 7. Real and imaginary part of dielectric constants of SnSe and $SnSe_2$ monolayers before and after the interfaces on graphene monolayer (SnSe@Graphene and $SnSe_2$@Graphene), and a both layers of graphene (Graphene@SnSe@Graphene and Graphene@$SnSe_2$@Graphene interfaces), as a function of THz.

monolayers and its heterostructures are even more interesting (in Fig. 6), in which by adding graphene monolayer on below of $SnSe_2$ structure, the optical band gap has transferred from 290 THz to 338 THz consisting of a very small peak between 24 and 48 THz. By adding another layer of graphene on SnSe@Graphene system, these two small peaks have shifted to 72 THz and 132 THz with higher adsorption

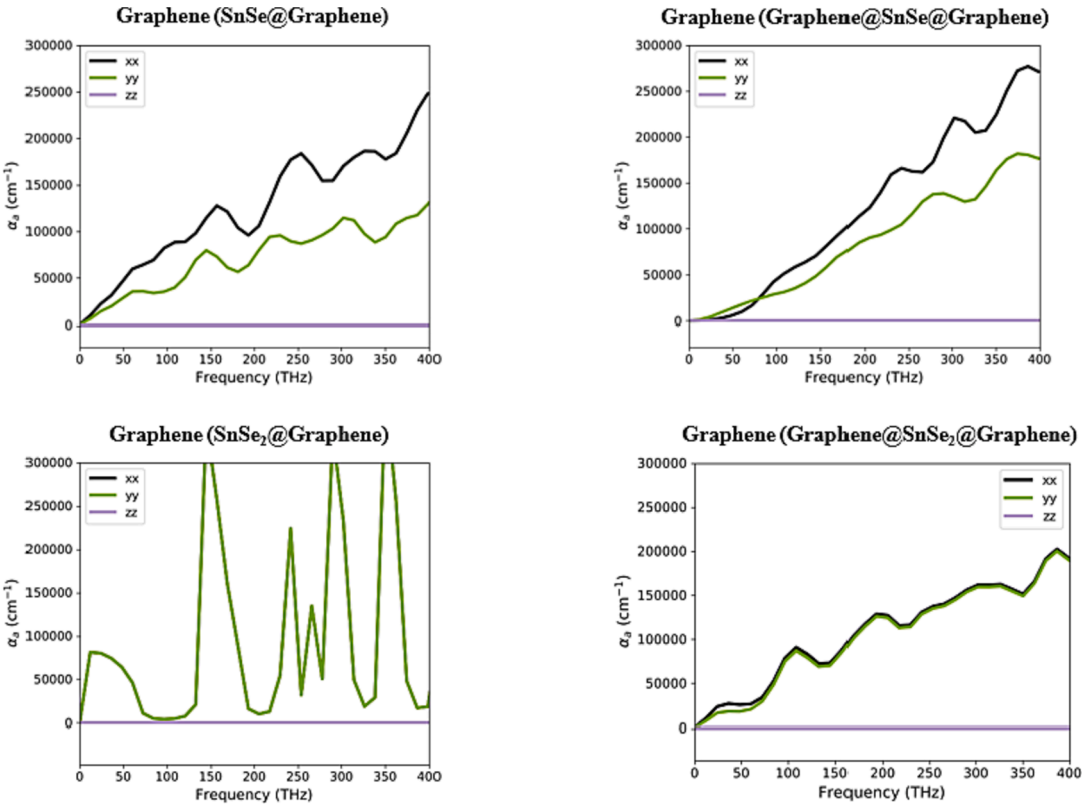

Fig. 8. Adsorption coefficient of graphene monolayer/monolayers after the interaction with SnSe and $SeSe_2$, reported in THz in SnSe@Graphene, $SnSe_2$@Graphene, Graphene@SnSe@Graphene, and Graphene@$SnSe_2$@Graphene.

intensity of 9316 cm^{-1} and 5713 cm^{-1}, respectively.

The results corresponded to dielectric constants of the real part and imaginary part (Fig. 7) can clearly explain our optical properties based on DFT calculations. Without any surprise, the THz imaginary part of the SnSe and $SnSe_2$ semiconductors are zero at their free-standing layers and SnSe@Graphene and $SnSe_2$@Graphene systems. This confirms that there are no free carriers present in both monolayers in this range. In Graphene@SnSe@Graphene and Graphene@$SnSe_2$@Graphene interfaces, the optical band gap in both SnSe and $SnSe_2$ are decreased, and the first peaks have shifted to vary low THz frequencies, in particularly for SnSe nanosheet which indicating their optical band gaps. These outcomes are strictly correlated to the absorption spectra of systems shown in Fig. 6.

Furthermore, as shown in Fig. 7, static dielectric constants were calculated to be 6.67, 6.91 and 3.90 for SnSe monolayer before the interface, and 1.92, 1.28 and 1.01 for SnSe in the system where present one monolayer of graphene, along with the in-plane and out-of-plane polarizations, respectively. Interestingly, adding two layers of graphene in both sides of SnSe, has remarkably enhanced it dielectric constant to 14.85, 29.39 and 1.65 along the same directions, respectively. Moreover, as shown in Fig. 7, the in-plane static dielectric constant of SnSe in Graphene@SnSe@Graphene indicated negative values in the range of 24–169 THz. Based on quantum theory of Drude model, this phenomenon may reveal that the surface plasmon polariton propagated in a parallel direction to the negative dielectric material interface [48,49]. About the $SnSe_2$ material, the static dielectric constant has changed from 4.57 and 3.36 in 2D $SnSe_2$ before the interface to 4.51 and 1.08 for $SnSe_2$ in $SnSe_2$@Graphene, and 1.92 and 1.01 to $SnSe_2$ in Graphene@$SnSe_2$@Graphene system.

After checking the absorption spectra and dielectric constant of SnSe and $SnSe_2$ materials in free standing and interfaces systems, we further examined the optical adsorption responses of the graphene monolayer/monolayers in four systems of SnSe@Graphene, $SnSe_2$@Graphene, Graphene@SnSe@Graphene, and Graphene@$SnSe_2$@Graphene. Different spectra related to graphene monolayers in Fig. 8 indicate that SnSe and $SnSe_2$ monolayers could not open the band gap of graphene after the interfaces and its metallic properties has been kept. Among different systems, graphene monolayer in $SnSe_2$@Graphene possesses its main first peak in lower frequencies of 12 THz, whereas this frequency in Graphene@$SnSe_2$@Graphene had shifted a bit to higher 24 THz. The same trend can be observed for graphene in SnSe@Graphene, and Graphene@SnSe@Graphene in which the first adsorption peak has shifted to higher frequencies when two layers of graphene have involved in the interface.

Conclusions

We investigated the electronic and optical properties of the SnSe and $SnSe_2$ structures as free-standing monolayers and in interfaces with graphene nanosheets by modelling SnSe@Graphene, $SnSe_2$@Graphene, Graphene@SnSe@Graphene, and Graphene@$SnSe_2$@Graphene heterostructures and using DFT calculations. Initially, we considered the electronic bandstructures of SnSe and $SnSe_2$ by using different methodologies in order to verify some available experimental measurements. While the results shown the semiconductor properties of SnSe and $SnSe_2$ with indirect bandgap of 1.20 eV and 0.94 eV calculated by traditional GGA and MGGA adopted PBE functional, hybrid HSE functional couldn't provide an accurate band gap for SnSe and $SnSe_2$ monolayers by overestimated values of 1.78 eV and 1.44 eV, respectively. The mobility and cc have examined for different thicknesses from monolayers to four layers for each material. While the results showed different trend among two structures having the same elements, the high mobility of 126×10^3 cm^2V^{-1} s^{-1} with cc of 1.3×10^{13} cm^3 for a two layers SnSe and 69×10^3 cm^2V^{-1} $s^{-1}$with cc of 4.2×10^{18} cm^3 for three layers $SnSe_2$, have predicted at room temperature.

More, the results of different interfaces indicate that the physical

origin of free-standing semiconductors of SnSe and $SnSe_2$ are highly sensitive to the number of graphene monolayers, since the interactions between the surfaces are covalent forces. By increasing the number of graphene layers putting on both sides of SnSe and $SnSe_2$ the band gap have been enhanced, and the total bandgap values have predicted to be 0.02 eV and 0.07 eV for SnSe@Graphene and $SnSe_2$@Graphene, and 0.2 eV and 1.08 eV for Graphene@SnSe@Graphene and Graphene@$SnSe_2$@Graphene, respectively. Also, we investigated the band gap of free-standing materials before/after the interfaces. By inserting one layer of graphene below the SnSe/$SnSe_2$ monolayers, their band gaps change from 1.20 eV/0.94 eV to 1.76 eV/1.13 eV, while adding the second layer of graphene in the upper part of SnSe@Graphene and $SnSe_2$@Graphene has significantly reduced their band gaps to 0.13 eV/0.4 eV, respectively, however, zero band gap of metallic graphene has been kept.

Further, the optical properties of different heterostructures and free-standing layers have been assessed and the results revealed that in Graphene@SnSe@Graphene and Graphene@$SnSe_2$@Graphene two adsorption peaks are observed at very low THz frequencies. Importantly, changing the dielectric constants of SnSe in Graphene@SnSe@Graphene from positive (0–24 THz) to negative values (24–169 THz), implying the occurrence of trapping electromagnetic radiation in present of the plasmons.

To conclude, we strongly suggest this specially designed heterostructures through the formation of the different semiconductor–metal materials applicable in fast electronic devices at GHz to THz frequencies.

Funding and Acknowledgments

This work is part of the research of HORIZON-EIC-2022-PATHFINDEROPEN-01 “Nano-scale Development of Plasmonic Amplifiers Based on 2D Materials” (PLASNANO) (grant agreement No. 101099552).

CRediT authorship contribution statement

Elaheh Mohebbi: Writing – review & editing, Writing – original draft, Visualization, Validation, Project administration, Methodology, Investigation, Data curation, Conceptualization. **Eleonora Pavoni:** Writing – original draft, Project administration. **Luca Pierantoni:** Writing – review & editing, Validation, Project administration. **Pierluigi Stipa:** Writing – review & editing, Supervision, Project administration, Conceptualization. **Gian Marco Zampa:** Project administration. **Emiliano Laudadio:** Writing – review & editing, Validation, Project administration, Methodology, Conceptualization. **Davide Mencarelli:** Writing – review & editing, Validation, Project administration.

Declaration of competing interest

The authors declare the following financial interests/personal relationships which may be considered as potential competing interests: Emiliano Laudadio reports financial support was provided by Polytechnic University of Marche. If there are other authors, they declare that they have no known competing financial interests or personal relationships that could have appeared to influence the work reported in this paper.

Data availability

No data was used for the research described in the article.

References

[1] Bafekry A, Faraji M, Fadlallah MM, Jappor HR, Karbasizadeh S, Ghergherehchi M, et al. Novel two-dimensional AlSb and InSb monolayers with a double-layer honeycomb structure: a first-principles study. Phys Chem Chem Phys 2021;23:18752–9.

[2] Almayyali AOM, Jappor HR, Muhsen HO. High hydrogen production in two-dimensional GaTe/ZnI2 type-II heterostructure for water splitting. J Phys Chem Solid 2023;178:111317.

[3] Bafekry A, Naseri M, Faraji M, Fadlallah MM, Hoat DM, Jappor HR, et al. Theoretical prediction of two-dimensional BC2X (X= N, P, As) monolayers: ab initio investigations. Sci Rep 2022;12:22269.

[4] Bafekry A, Faraji M, Karbasizadeh S, Sarsari IA, Jappor HR, Ghergherehchi M, et al. Two-dimensional FeTe 2 and predicted Janus FeXS (X: Te and Se) monolayers with intrinsic half-metallic character: Tunable electronic and magnetic properties via strain and electric field. Phys Chem Chem Phys 2021;23:24336–43.

[5] Mohebbi E, Fakhrabadi MMS. Investigation of stability, electronic, optical and mechanical properties of honeycomb BeN2 monolayer: A DFT study. Comput Theor Chem 2023:114202.

[6] Ramasamy P, Manivasakan P, Kim J. Phase controlled synthesis of SnSe and SnSe 2 hierarchical nanostructures made of single crystalline ultrathin nanosheets. CrstEngComm 2015;17:807–13.

[7] Padha N, Kumar S. A two-step method to obtain the 2D layers of SnSe 2 single phase and study its physical characteristics for photovoltaic and photo-converter devices. Appl Phys A 2021;127:1–13.

[8] Chung K-M, Wamwangi D, Woda M, Wuttig M, Bensch W. Investigation of SnSe, SnSe2, and Sn2Se3 alloys for phase change memory applications. J Appl Phys 2008;103.

[9] Barrios-Salgado E, Nair MTS, Nair PK. Chemically deposited SnSe thin films: thermal stability and solar cell application. ECS J Solid State Sci Technol 2014;3:Q169.

[10] Gupta SU, Dalvaniya AG, Patel NF, Bhakhar SA, Nair S, Joy J, et al. Optical switching device based on a crystalline SnSe2 photodetector in diverse conditions. ACS Appl Electron Mater 2021;3:4859–69.

[11] Kumar M, Rani S, Vashishtha P, Gupta G, Wang X, Singh VN. Exploring the optoelectronic properties of SnSe: a new insight. J Mater Chem C Mater 2022;10:16714–22.

[12] Shi W, Gao M, Wei J, Gao J, Fan C, Ashalley E, et al. Tin selenide (SnSe): growth, properties, and applications. Adv Sci 2018;5:1700602.

[13] Kumar M, Rani S, Singh Y, Gour KS, Singh VN. Tin-selenide as a futuristic material: properties and applications. RSC Adv 2021;11:6477–503.

[14] Mulla R, White AO, Dunnill CW, Barron AR. The role of graphene in new thermoelectric materials. Energy Adv 2023;2:606–14.

[15] Novoselov KS, Mishchenko A, Carvalho A, Castro Neto AH, 2D materials and van der Waals heterostructures, Science (1979) 353 (2016) aac9439.

[16] Torres-Rojas RM, Contreras-Solorio DA, Hernández L, Enciso A. Band gap variation in bi, tri and few-layered 2D graphene/hBN heterostructures. Solid State Commun 2022;341:114553.

[17] Yu L, Lee Y-H, Ling X, Santos EJG, Shin YC, Lin Y, et al. Graphene/MoS2 hybrid technology for large-scale two-dimensional electronics. Nano Lett 2014;14:3055–63.

[18] Wang Z, Chen Q, Wang J. Electronic structure of twisted bilayers of graphene/MoS2 and MoS2/MoS2. J Phys Chem C 2015;119:4752–8.

[19] Lu C, Quan C, Si K, Xu X, He C, Zhao Q, et al. Charge transfer in graphene/WS2 enhancing the saturable absorption in mixed heterostructure films. Appl Surf Sci 2019;479:1161–8.

[20] Alsalama M, Hamoudi H, Abdala A, Youssef KM. Effect of graphene on thermal stability of tin selenide. J Mater Res Technol 2022;18:896–908.

[21] Mohebbi E, Pavoni E, Pierantoni L, Stipa P, Laudadio E, Mencarelli D. Effect of different pseudopotentials on the phonon frequencies, dielectric constant, and Born effective charge of SnSe and SnSe2 nanostructures: A density functional perturbation theory study. J Phys Chem Solid 2023:111755. https://doi.org/10.1016/j.jpcs.2023.111755.

[22] Smidstrup S, Markussen T, Vancraeyveld P, Wellendorff J, Schneider J, Gunst T, et al. QuantumATK: An integrated platform of electronic and atomic-scale modelling tools. J Phys Condens Matter 2019;32:015901.

[23] Pavoni E, Mohebbi E, Stipa P, Pierantoni L, Mencarelli D, Dragoman M, et al. First-principles investigation of interface phenomena in hafnium-based metal–insulator–metal diodes. Nanoscale Adv 2023;5:2748–55.

[24] Laudadio E, Mohebbi E, Pavoni E, Minnelli C, Sabbatini S, Stipa P. Density functional theory and molecular dynamics studies on electrical, mechanical, and thermal properties of TiO2 nanoparticles interacting with poly lactic-co-glycolic acid. Colloids Surf A Physicochem Eng Asp 2023;667:131388.

[25] Mohebbi E, Pavoni E, Pierantoni L, Stipa P, Laudadio E, Mencarelli D. Insights into a new geometric graphene diode with ultrahigh asymmetry ratio: A computational approach. In: 2023 IEEE 23rd international conference on nanotechnology (NANO); 2023. p. 238–42.

[26] Kohn W, Sham LJ. Self-consistent equations including exchange and correlation effects. Phys Rev 1965;140:A1133.

[27] Ernzerhof M, Scuseria GE. Perspective on “Inhomogeneous electron gas” Hohenberg P, Kohn W (1964) Phys Rev 136: B864. Theor Chem Acc 1964;103(2000):259–62.

[28] Sánchez-Portal D, Ordejon P, Artacho E, Soler JM. Density-functional method for very large systems with LCAO basis sets. Int J Quantum Chem 1997;65:453–61.

[29] van Setten MJ, Giantomassi M, Bousquet E, Verstraete MJ, Hamann DR, Gonze X, et al. The PseudoDojo: Training and grading a 85 element optimized norm-conserving pseudopotential table. Comput Phys Commun 2018;226:39–54.

[30] Wan Z, De Wang Q, Liu D, Liang J. Effectively improving the accuracy of PBE functional in calculating the solid band gap via machine learning. Comput Mater Sci 2021;198. https://doi.org/10.1016/j.commatsci.2021.110699.

[31] Ehrlich S, Moellmann J, Reckien W, Bredow T, Grimme S. System-dependent dispersion coefficients for the DFT-D3 treatment of adsorption processes on ionic surfaces. ChemPhysChem 2011;12:3414–20.
[32] Haas P, Tran F, Blaha P, Schwarz K. Construction of an optimal GGA functional for molecules and solids. Phys Rev B 2011;83:205117.
[33] Goll E, Ernst M, Moegle-Hofacker F, Stoll H. Development and assessment of a short-range meta-GGA functional. J Chem Phys 2009;130.
[34] Henderson TM, Paier J, Scuseria GE. Accurate treatment of solids with the HSE screened hybrid. Physica Status Solidi (B) 2011;248:767–74.
[35] Mohebbi E, Pavoni E, Mencarelli D, Stipa P, Pierantoni L, Laudadio E. Insights into first-principles characterization of the monoclinic VO 2 (B) polymorph via DFT+ U calculation: electronic, magnetic and optical properties. Nanoscale Adv 2022;4:3634–46.
[36] Mohebbi E, Fakhrabadi MMS. Electronic, optical, mechanical, and thermal properties of diphenylacetylene-based graphyne nanosheet using density functional theory. Nanotechnology 2021;32:405705.
[37] Martin RM. Electronic structure: basic theory and practical methods. Cambridge University Press; 2020.
[38] D.J. Griffiths, Introduction to Electrodynamics Fourth Edition, (2021).
[39] Gunst T, Markussen T, Stokbro K, Brandbyge M, First-principles method for electron-phonon coupling and electron mobility: Applications to 2D materials, ArXiv Preprint ArXiv:1511.02045 (2015).
[40] Parenteau M, Carlone C. Influence of temperature and pressure on the electronic transitions in SnS and SnSe semiconductors. Phys Rev B 1990;41:5227.
[41] Rajesh S, Parvathi MM, Mohan A, Arivazhagan V. Preparation and characterization of vacuum evaporated SnSe and SnSe2 multilayer thin films. AIP Conf Proc, American Institute of Physics; 2012. p. 206–8.
[42] Lu D, Yue C, Luo S, Li Z, Xue W, Qi X, et al. Phase controllable synthesis of SnSe and SnSe2 films with tunable photoresponse properties. Appl Surf Sci 2021;541:148615.
[43] Kumar M, Rani S, Pandey A, Gour KS, Husale S, Singh P, et al. Highly responsive, low-bias operated SnSe2 nanostructured thin film for trap-assisted NIR photodetector. J Alloys Compd 2020;838:155384.
[44] Zhou M, Chen X, Li M, Du A. Widely tunable and anisotropic charge carrier mobility in monolayer tin (II) selenide using biaxial strain: a first-principles study. J Mater Chem C Mater 2017;5:1247–54.
[45] Wang S, Hui S, Peng K, Bailey TP, Liu W, Yan Y, et al. Low temperature thermoelectric properties of p-type doped single-crystalline SnSe. Appl Phys Lett 2018;112.
[46] Liang T, Hu C, Lou M, Feng Z, Wang D, Cai X, et al. High carrier mobility and controllable electronic property of the h-BN/SnSe2 heterostructure. Langmuir 2023;39:10769–78.
[47] Liu M, Zhang J, Xu J, Hu B, Liu B, Sun K, et al. Phase structure, phase transition and thermoelectric properties of pristine and Br doped SnSe2. J Solid State Chem 2020;289:121468.
[48] Zeng S, Yu X, Law W-C, Zhang Y, Hu R, Dinh X-Q, et al. Size dependence of Au NP-enhanced surface plasmon resonance based on differential phase measurement. Sens Actuators B Chem 2013;176:1128–33.
[49] Das S, Kumar R, George TJ, Bansal A, Lautre NK, Sharma AK. Physics of electrostatic resonance with negative permittivity and imaginary index of refraction for illuminated plasmoid in the experimental set up for microwave near field applicator, Fundam. J Mod Phys 2013;5:19–46.